

In-Situ Thermal Image Correlation with Mechanical Properties of Nylon-12 in SLS

Walker Wroe, Jessica Gladstone, Timothy Phillips, Austin McElroy, Scott Fish, Joseph Beaman

The University of Texas at Austin
Mechanical Engineering Department, Cockrell School of Engineering
Austin, TX
Email: walkerwroe@gmail.com

Abstract

Selective laser sintering (SLS) of Nylon is a significant portion of the additive manufacturing market for structurally sensitive applications. Current methods of acceptance for such parts are based on the inclusion of ASTM tensile test specimens within the build volume to assess the overall build quality. Ultimate strength and elongation of these specimens oriented both in-plane and normal to the layer build direction are the primary quality metrics. This paper looks at a more complete method of certifying parts for acceptance based on examination of the build conditions in each layer of the part by comparing layer-by-layer thermal conditions during the part build to the resulting ASTM specimen tensile properties. Through such a comparison, a more complete three-dimensional assessment of part quality during the build process can be constructed. The layer-by-layer assessment used here is derived from infrared thermal imaging; mapping temperature profiles of SLS-built tensile bars with data collected before, during, and after each layer-wise laser melting sequence. Mechanical properties and fracture conditions are then quantified and correlated with the conditions where the fractures occur. Build conditions associated with poor failure conditions may then be used to assess poor SLS bonding throughout the part volume, improving overall part quality assessment and certification. As the method is matured, real time layer-by-layer assessment will be linked to SLS control, to correct for observed defects during the build and improve overall part quality and repeatability.

1. Introduction

Although a number of Additive Manufacturing (AM) technologies exist, Selective Laser Sintering (SLS) remains one of the most versatile of these methods for building structurally efficient products. The SLS process creates a three-dimensional part, layer-by-layer, from powder that is melted using a laser. This method is particularly useful for complex geometries without the need (in plastics) for support structures. Although SLS has been in use for prototyping and low stress part production since the late 1980's, further research and development is needed to achieve consistent high mechanical performance in manufacturing applications.

For parts manufactured with layer-by-layer accumulation of material (including SLS), the weakest direction is often in the direction perpendicular to the layers, which will be referred to in this paper as the Z-Axis^{1,2}.

One important process-based issue in SLS is consistent control of thermal conditions during the build. Inconsistent melt and re-solidification conditions can give rise to unpredictable structural results, due to unwanted porosity, and poor bonding between

melt regions both in and between layers. Process monitoring of such issues is essential to understanding their relative importance. [3 (Yuan), 4(Wegner)]

The Laser Additive Manufacturing Pilot System (LAMPS) is a valuable SLS research machine, developed to easily add or modify measurement and control tools. Visual and infrared (IR) cameras are currently used for in-situ process monitoring as will be described further in this paper. The IR camera is oriented to provide simultaneous thermal measurement of the build surface and powder prior to spreading over the build surface for control of these temperatures independently from the same image sensor source.

With this experimental capability, correlations can be drawn between the thermal history of parts built and their corresponding tensile test results. The focus for this paper on Z-axis tensile bars enables direct comparison of interlayer bonding characteristics under different build thermal conditions with the mechanical properties of ASTM class specimens. Once this correlation is well characterized, such comparisons can be made (and control compensation implemented) for separate 3D parts.

2. LAMPS Machine and Tensile Test Specimens

The LAMPS (Laser Additive Manufacturing Pilot System) machine was designed and built at the University of Texas at Austin for the study of SLS process control and its extension to existing and new polymer based materials. LAMPS provides direct access to all measurements for both monitoring and control. Controls are implemented in an open architecture using National Instruments LabVIEW based software tools. Users have control over all process parameters, and are able to add and remove data acquisition elements as needed. For this paper, the primary thermal sensor is a long wave infrared (IR) camera (*FLIR A325*), mounted as shown in Figures 1 and 2. A more complete description of the LAMPS System can be found in Fish et.al.²

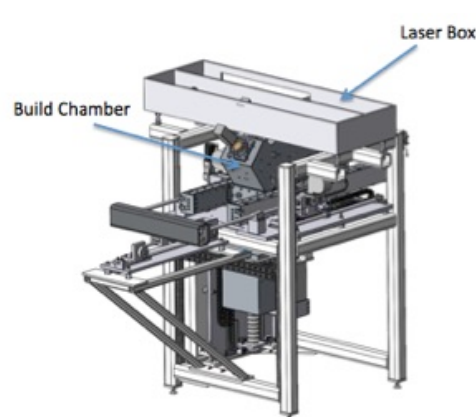


Figure 1 – LAMPS External View

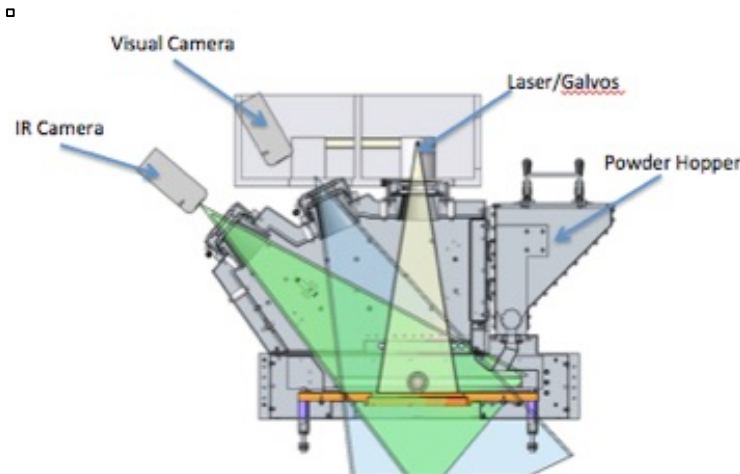


Figure 2 – LAMPS Build Chamber Cross Section

The baseline control use of the IR camera is for real time closed loop control of a pair of quartz lamps that act as a secondary heating source for the build surface and pre-spread powder drop zones. Background heating of the build is achieved by controlling the atmospheric temperature with an array of wall and build plate mounted heaters. The atmosphere for this experiment is Nitrogen. The IR camera also captures thermal images of the build surface during the laser scan for analysis of thermal conditions of the part layers as they are built, which is the focus of this paper. The images captured for this work at 30 frames per second, over an average scan time of 20 seconds per layer. The tensile specimens for this paper required 712 layers, requiring over 150 GB of data for the entire build.

3. Specimen Build and Corresponding Image Analysis

In order to perform a direct and consistent comparison between various SLS-built specimens, ASTM Type I tensile specimens with slightly shorter gauge lengths were built as shown in Figure 3. To assess layer-to-layer bonding characteristics, the specimens were oriented perpendicular to the layer plane in 3 rows of 10 specimens each. All specimens were numbered based on their location (row/column) in the build for comparison/correlation with in-situ IR measurements.

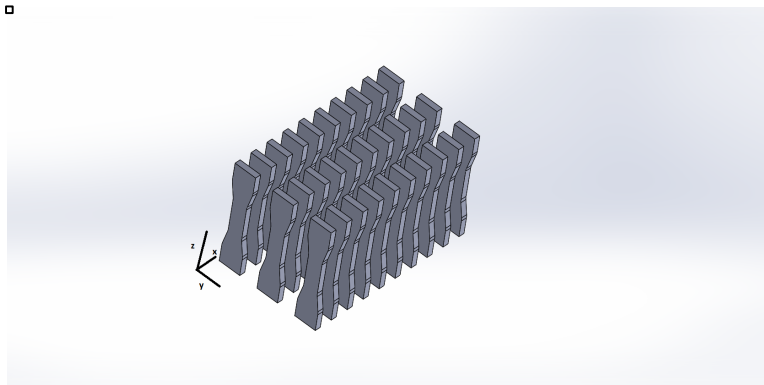


Figure 3 - Tensile specimen orientation for this study

IR data was captured for each layer of the build for the complete period of laser operation. Each image was then processed with an image filter [5] to adjust (keystone affect) for the angle offset from the IR camera's mounting and to align image pixel data with the reference frame of the parts as scanned by the laser. A depiction of the filter's impact on the IR images is shown below in Figure 4. In this figure, the left image is the raw image taken by the IR camera, while the right image is the adjusted image in MATLAB, which accounts for the laser scan reference frame. Additionally, to reduce the amount of stored data, a cropping tool was used to only include the sintered geometries and their immediate surrounding surface.

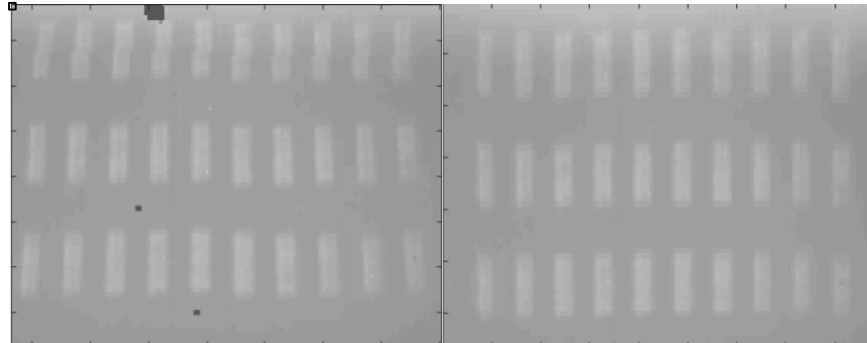


Figure 4 - Image keystone filtering

Once the filter is applied, appropriate regions of interest (ROI) were designated corresponding to the areas sintered for each specimen. Figure 5 shows the arrangement of these ROI in the three rows of 10 as built in the LAMPS system with row 1 being farthest from the hopper/start of spreading, and closer to the dump side of the build. For each frame of data, an average temperature is determined for each ROI.

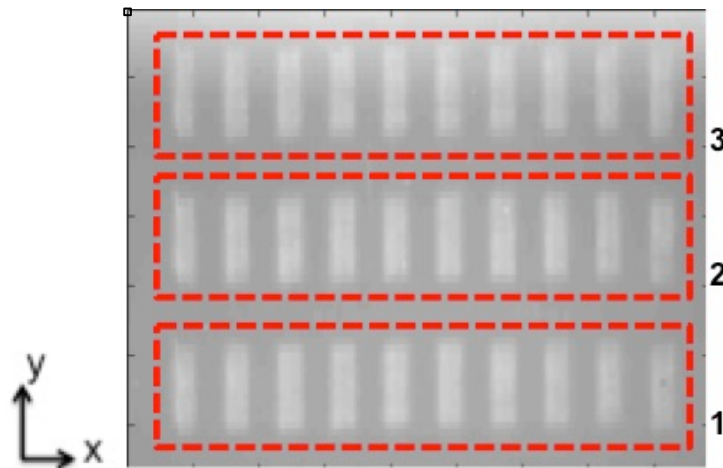


Figure 5 – Row references in the corrected data image

Figure 6 shows a time-averaged contour map from the corrected imagery for all pixels within a single layer. The elevated humps in this figure correspond to the ROI's for each specimen, and one can see that the background temperature is higher above the 3rd row. This perceived higher background temperature is likely due to radiation bleed

around a shield between one of the quartz lamps and the IR camera and may be biasing the ROI derived temperatures for the 3rd row of specimens.

□

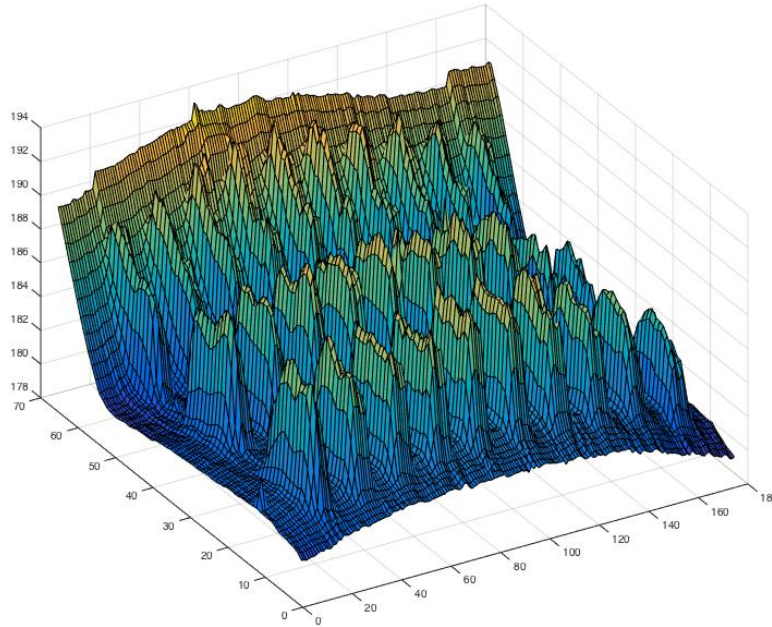


Figure 6 - Build surface temperatures averaged over one layer scan period

After all images were captured for a single layer, a temperature matrix was built for the array of specimens corresponding to several key conditions within a layer. The first is an average temperature for each ROI over the complete scan time (as shown in Figure ** above). We also extracted a representative temperature for each ROI just before it was scanned and just after it's scan exposure was completed as described in Section 4.

During the build process, the laser scanned in alternating directions by layer number as is common for commercial scanning practice, as shown in Figure 7. For odd layers, starting at Layer 1, the laser scans or "marks" in the positive x-direction, and then jumps back and repeats this movement at the next higher value of y based on the scan separation distance. For even layers, the laser scans in the positive y-direction and then repeats with the scan offset increasing in x.

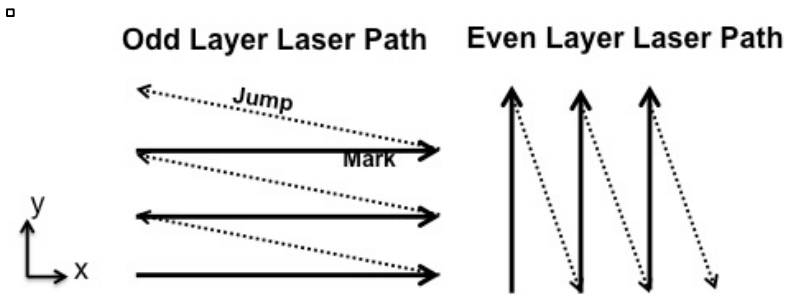


Figure 7 - Laser scanning pattern by layer number

4. Description of Thermal Imaging Analysis

In addition to the average temperature of each specimen's layer over the complete scan period, an estimate of the temperature just prior to scan and just after the scan is also desired for correlation with observed mechanical properties. The image frames within a layer for these conditions were found as follows. First, the frame-by-frame temperature of each specimen over the layer scan period is gathered. Examples of this temporal variation for two specimens are plotted in Figure 8 for an odd layer. ROI 1 corresponds to the first specimen in the 1st row and ROI 11 corresponds to the first specimen in the 2nd row (See previous ROI Figure 5 for reference). When an image frame captures the laser scanning the ROI of interest, the associated average temperature for that ROI jumps out of range due to the very high reflection in the IR band for the CO₂ laser being used. One can nevertheless follow the effective average temperature by ignoring these frames as illustrated in Figure 8. The frame where and ROI first jumps is a good indication of when scanning starts for that specimen and the previous frame is used as its "pre-scan" temperature. For odd layers, each row is effectively finished scanning when the next row scanning starts, so the frame taken when ROI 11 temperature jumps out of range (in row 2) is selected for evaluation of "post scan" temperatures for all specimens in row 1.

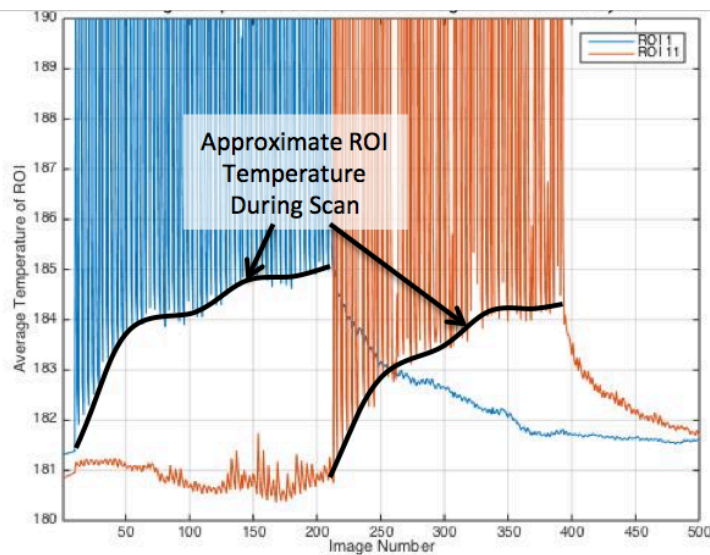


Figure 8 - Sample image frame based temperature history for two specimens (ROI) for a single layer scan.

Pre and post scan temperatures were thus gathered for all specimens over all layers of the build.

5. Mechanical and Thermal Results

All thirty specimens were tensile tested using standard ASTM 638 methodology using an Instron 3345 tensile machine and the resulting stress vs. strain curves for each are shown in Figure 9. All specimens fractured within the gauge length, except for the weakest specimen, which fractured in two places simultaneously. The near vertical lines at maximum extension aid in visualizing the strain at break for each specimen.

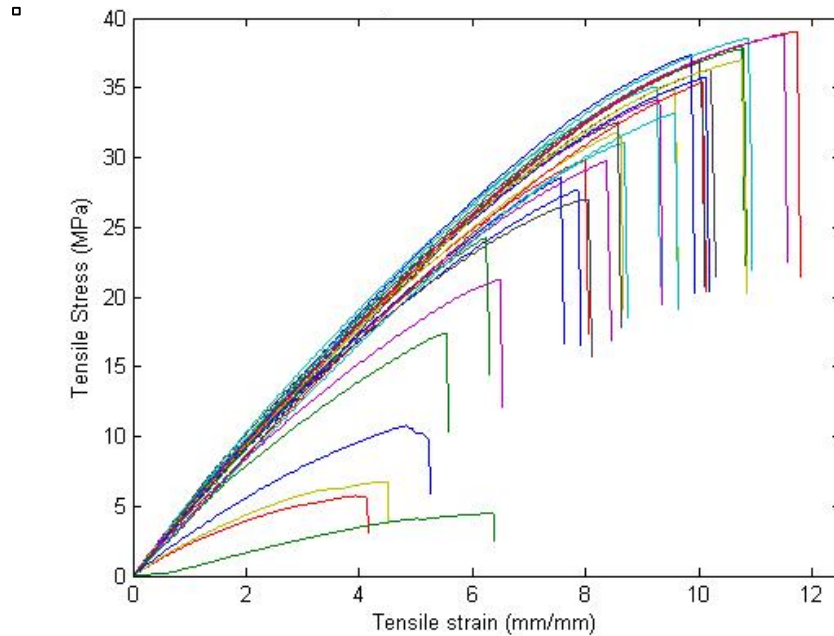


Figure 9 - Measured stress vs. strain for all 30 tensile specimens

The weakest specimens corresponded to the lower average temperature regions in the build, which were located on the ends of each row as shown in Figure 5, from Section 3. A more thorough study of spatial variation in specimens will be covered in a future paper. The first comparison uses the average temperature over the full scan time of all layers and the corresponding fracture strength as shown in Figure 10. Other than the two specimens at 185.1 and 185.5 C, there appears to be a break in the strength behavior of the group at around 186.5 C. Linear fits to the data (excluding the two points mentioned above) above and below this break are shown suggest that the fracture strength drops off by 75% or more if the average temperature does not reach the break point. Further discussion of this can be found in Section 6. A significant increase in strength, as the average temperature is increased, is seen in the higher strength portions of Figure 10.

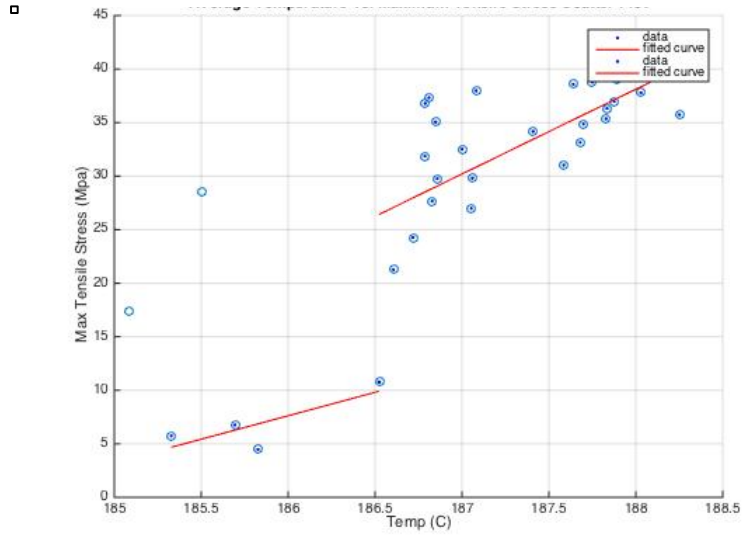


Figure 10 - Specimen “scan time” average temperature vs. fracture stress

Figures 11 and 12 show the similar correlation for pre-sintering and post sintering temperatures averaged over all layers, for each specimen versus its fracture strength. The correlation with pre sintering is obviously poor, while the post sintering temperature shows a two-zone characteristic similar to that with the overall average layer temperature described previously. The post sintering temperature, which should be a more direct measurement of layer melt and bonding quality, does not show as strong a correlation with fracture strength as the scan averaged data of Figure 10, and also shows significant variation in strength around the transition temperature between low and high strength specimens.

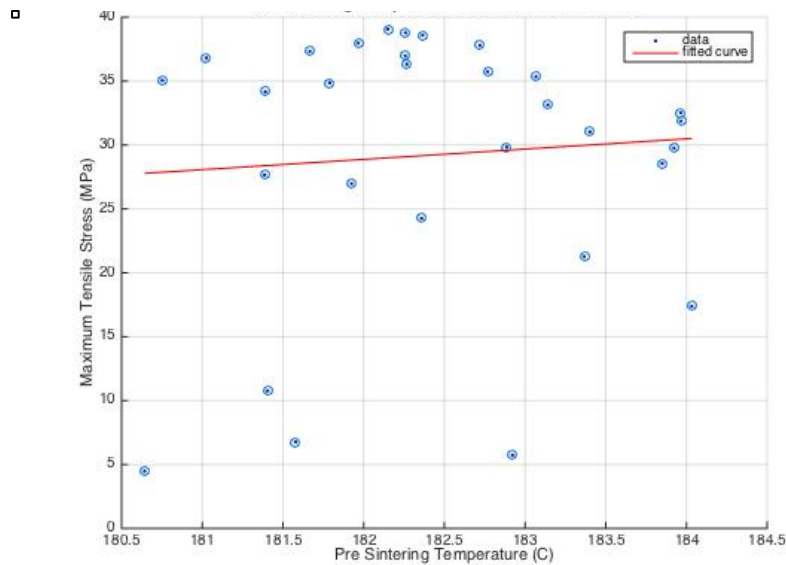


Figure 11 - Averaged pre-sintering temperature vs. fracture stress

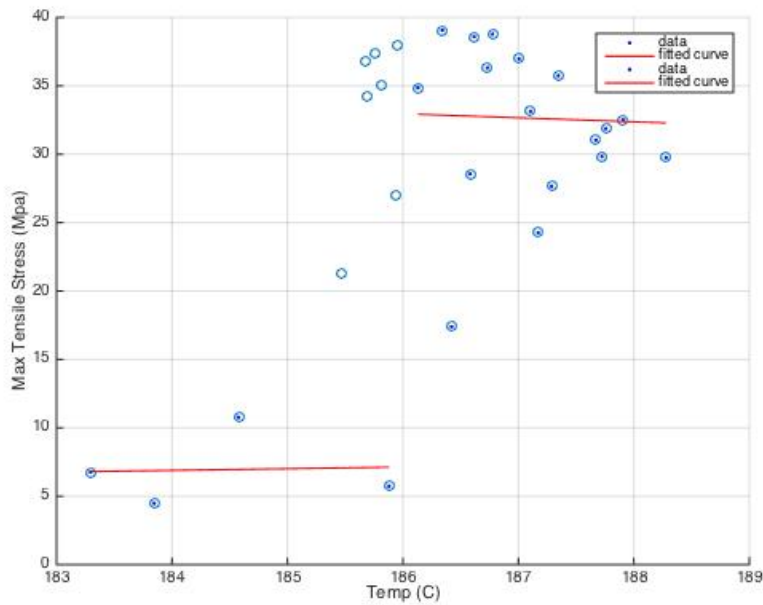


Figure 12 - Averaged post-sintering temperature vs. fracture stress

Correlations between the strain at break and the pre- and post- sintering layer averaged temperatures are shown Figures 13 and 14, respectively, and follow the nature of the strength data.

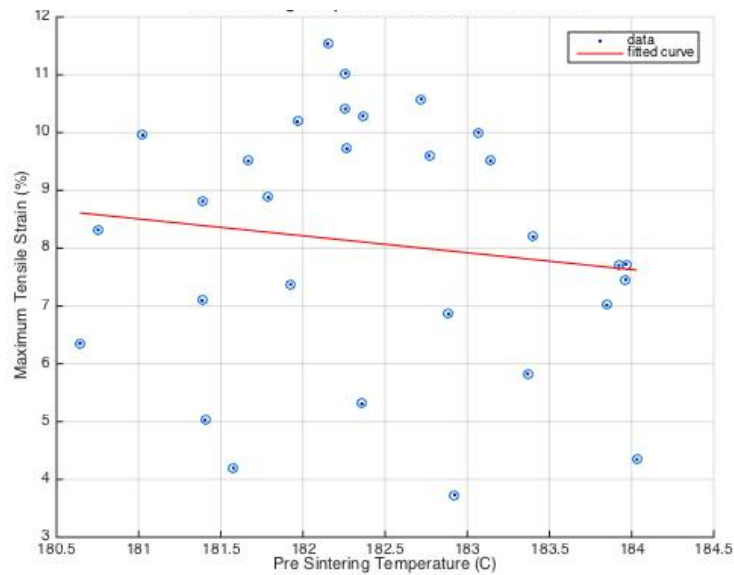


Figure 13 - Average pre-sintering temperature vs. strain at break

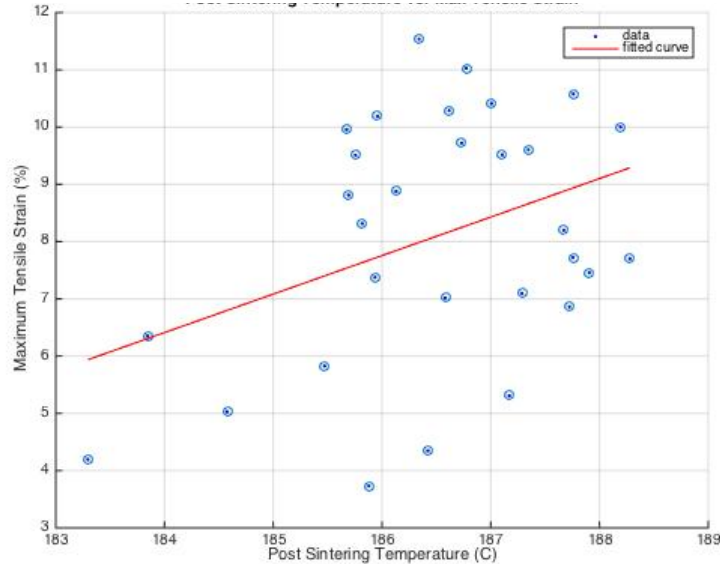


Figure 14 - Average post-sintering temperature vs. strain at break

Although the trend is not as obvious as that of the tensile stress plots, it is still clear that the post-sintering temperature of a specimen plays a bigger role in the maximum tensile strain. For low post-sintering temperatures, the tensile strain is only 4-7%, while at higher post-sintering temperatures; the strain can nearly be doubled, at about 10-12%.

It is believed that the reason the above correlations are not very strong is that by averaging over an entire ROI (35 pixels), the initially local nature of delamination between layers can be washed out. In order to identify these local defects a new analysis strategy was implemented where the minimum average temperature of every 3x3 pixel area in each ROI was taken from the post-sintering image and chosen as the temperature to represent that layer. The minimum value of all the layers was then taken to represent the temperature value for that specimen and is called the local-minimum post-sintering temperature. Figure 15 below gives a visual description of the 3x3 regions in each ROI, and Figure 16 shows the plot of the local-minimum post-sintering temperature versus ultimate tensile strength. This new comparison gives a much stronger correlation of .746, with the correlation between the local-minimum post-sintering temperature and tensile strain at break being .724.

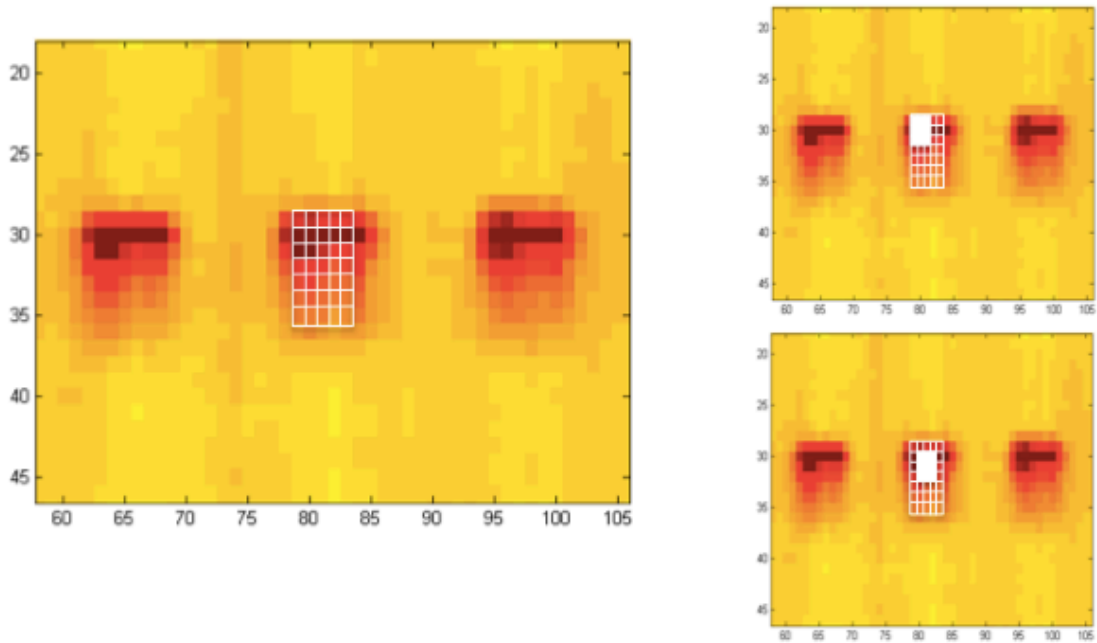


Figure 15 – Finding local-minimum post-sintering temperature

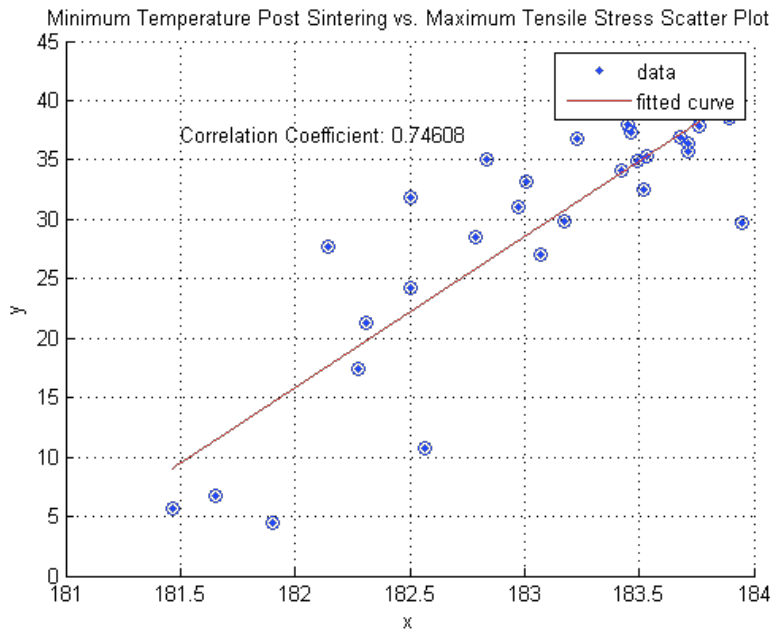


Figure 16 – Local-minimum post-sintering vs. ultimate tensile strength

6. Examination of Specimen Fracture Characteristics

Additionally, due to the poor layer-to-layer bonding experienced in z-direction builds, the specimens all notably broke with brittle characteristics and well aligned with the layer orientations. Figure 17 shows sample images of a strong and weak break, respectively. It is difficult at this scale to see differences in the break characteristics but

we expect a closer examination would reveal characteristics of unmelted powder in the lower strength samples.



Figure 17 - Sample fracture images for low and high strength specimens

7. Localized Layer Temperature vs. Fracture Correlation

All sample fracture locations were measured and linked to a build layer number. This was accomplished by measuring the distance from the bottom of the specimen to the fracture with an uncertainty of ± 2.5 mm estimated from material ejection during fracture and caliper accuracy. This corresponds to a layer uncertainty band of ± 30 layers in the build. Figures 18 and 19 show examples of both positive and negative correlation between thermal and mechanical layer failure criteria performed for each specimen using the method described below. The process begins by taking each layer's average temperature and non-dimensionalizing it as a percent difference from the overall layer mean value. Note that the raw layer temperature data are clumped either above or below the mean temperature with few being close to the mean value. This difference in temperature is a result of increased energy deposition by the laser at the beginning and end of each "mark" through a specimen. Because odd layers have this increase over the long sides of the rectangular area of each specimen, they have a slightly higher temperature over the ROI than for even layers which have the narrow edges getting more laser energy.

A low pass filter with a pass-band frequency of 0.1, corresponding to a blending of 10 layers, mitigates this oscillation and captures general trends in the temperatures of the specimen as a function of layer. In the figures, individual layer data is shown with circles and the filtered data shown with a solid curve. The different energy density levels in even and odd layers need further investigation, but an initial compensation has been examined with results shown in Figures 20 and 21 for the same data as shown in Figures 18 and 19. In this new view, odd and even layer deviations are shown from their respective mean values. This reduces the layer-to-layer oscillation and allows for a higher frequency low pass filter of 0.25, corresponding to blending of 4 layers, and a more direct examination of unusually cool layer temperatures compared with their averages. From the filtered thermal layer data, we extract the layer number where the lowest ten-layer blended temperature occurs, which is shown as the red circle icon on the curve. This is based on an assumption that failure will occur close to the layers with the lowest collective melting and bonding. This lowest temperature layer is then compared with the band of potential failure layers from the mechanical measurement, shown in yellow band in the figure. If the thermal estimate of weakest layer falls within the band of mechanical failure measurement, it is considered potentially correlated.

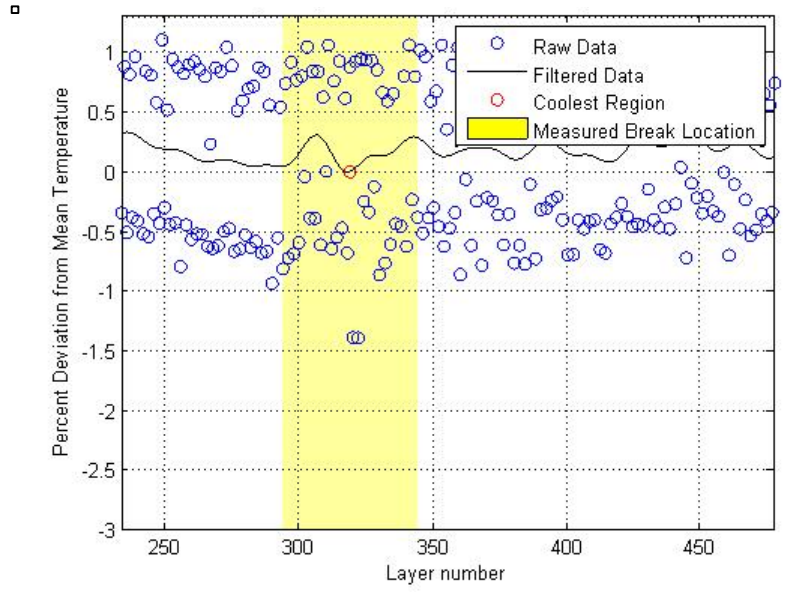


Figure 18 - Potentially correlated thermal and mechanical layer failure conditions

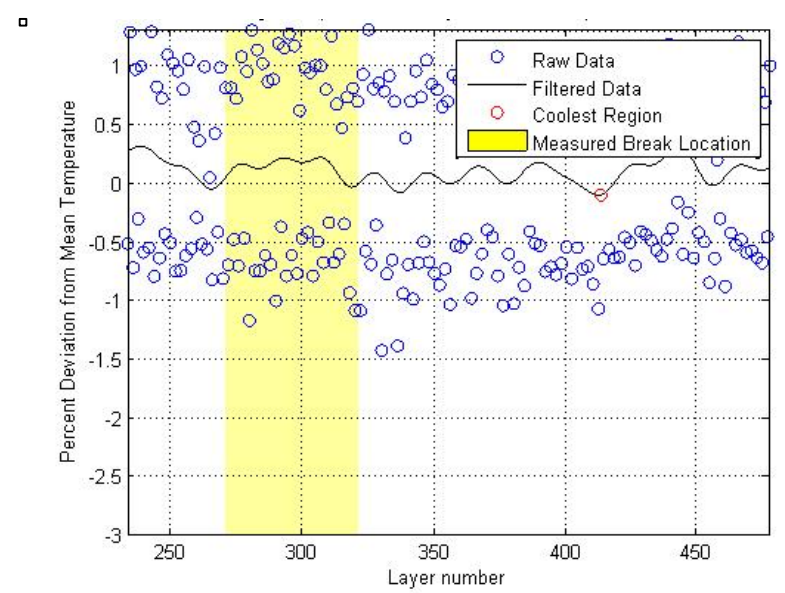


Figure 19 – Non-correlated thermal and mechanical layer failure conditions

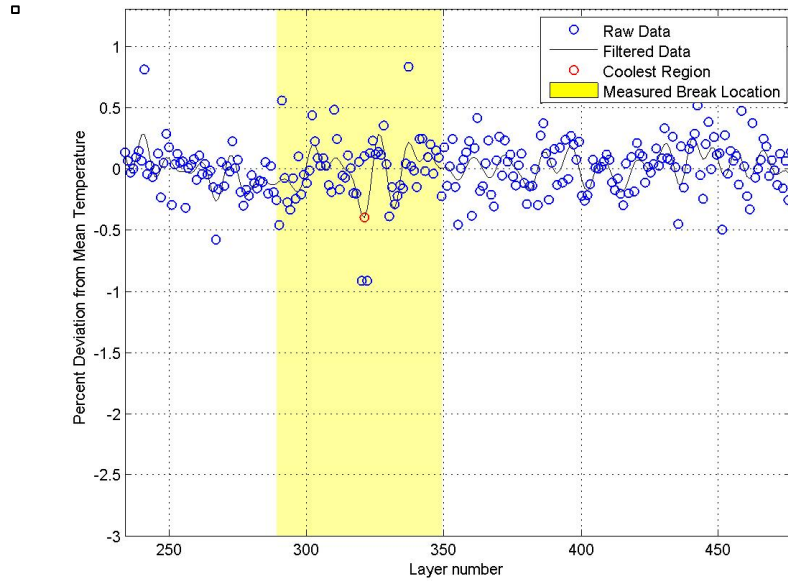


Figure 20 - Potentially correlated thermal and mechanical layer failure conditions

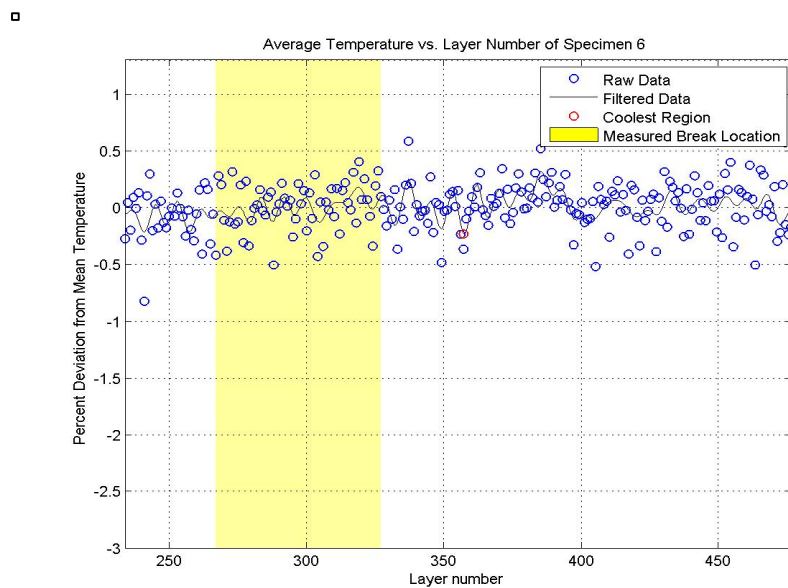


Figure 21 - Non-correlated thermal and mechanical layer failure conditions

Using these criteria, 12 out of 26 specimens were correlated in thermal and mechanical layer failure, a success rate of 46%, while randomly choosing points for suspected break location results in a success rate of 20%. Although this percentage is not ideal, it suggests that further examination of the criteria and improved measurement could lead to useable correlation of thermal conditions to break likelihood.

The local-minimum post-sintering temperature for each layer was also used to predict the break location but the success rate fell to 35 % against an expected random success rate of 16 %. This decrease in the random predicted success rate is due to a

tightening of the success band, the yellow region in the above figures, from +/- 30 layers to +/- 20 layers.

8. Conclusion

In-situ measurement of the thermal properties of the laser sintered surfaces throughout the build process was analyzed and compared with the mechanical failure stress and elongation of resulting tensile specimens. The results show correlation between the average temperature of the sintered layers and the strength and elongation with a threshold for this average temperature, below which poor performance is noted. Pre-sintering layer temperatures were not found to correlate well with fracture strength or strain at break. Correlation of fracture strength and elongation was not found with the pre-sintering layer temperature, and the correlation with post sintering temperatures was surprisingly low, given the overall average temperature correlation. When more local temperatures were looked at the correlations did improve significantly to about .74. Initial study of targeting weaker layer regions based on lower thermal measurement looks promising, improved quality of laser scanning control is needed to provide predictive consistency.

Future work to improve this prediction will involve closer control of laser power at the beginning and end of “marking” vectors. This can be accomplished by working with a laser with a more uniform laser energy density. Additionally, increasing the time resolution during the scan to better resolve the average temperatures of interest can make improvements to the results. Closer examination of the fracture samples will also be used to better document post fracture inter-layer conditions for comparison with thermal data from the build in the local region of failure.

Acknowledgment

This work is sponsored by the Air Force Research Lab and General Dynamics Information Technology (GDIT) under GDIT Prime Contract FA8650-11-D-5702 / 0009.

Citations

1. Yuan, M., and D. Bourell. "Efforts to Reduce Part Bed Thermal Gradients during Laser Sintering Processing." Proc. of 23rd Annual International Solid Freeform Fabrication Symposium, Austin, Tx. N.p.: n.p., n.d. N. pag. Print.
2. Fish, S. S. Kubiak, A. Bryant, J. Beaman, W. Wroe, and J. Booth, “A High Temperature Polymer Selective Laser Sintering Testbed for Controls Research”, Solid Freeform Fabrication Symposium, August 2015.
3. A. Wegner and G. Witt, “Process monitoring in laser sintering using thermal imaging,” presented at the SFF Symposium, Austin, Texas, USA, 2011, pp. 8–10.
4. “<http://www.mathworks.com/help/images/ref/imtransform.html>”